Comparison of Nonlinear Local Lyapunov Vectors and Bred Vectors in Estimating the Spatial Distribution of Error Growth

JIE FENG

School of Meteorology, University of Oklahoma, Norman, Oklahoma

JIANPING LI

State Key Laboratory of Earth Surface Processes and Resource Ecology, College of Global Change and Earth System Science, Beijing Normal University, Beijing, and Laboratory for Regional Oceanography and Numerical Modeling, Qingdao National Laboratory for Marine Science and Technology, Qingdao, China

RUIQIANG DING

State Key Laboratory of Numerical Modeling for Atmospheric Sciences and Geophysical Fluid Dynamics, Institute of Atmospheric Physics, Chinese Academy of Sciences, and College of Earth Science, University of Chinese Academy of Sciences, Beijing, China

ZOLTAN TOTH

Global Systems Division, NOAA/OAR/ESRL, Boulder, Colorado

(Manuscript received 5 September 2017, in final form 24 January 2018)

ABSTRACT

Instabilities play a critical role in understanding atmospheric predictability and improving weather forecasting. The bred vectors (BVs) are dynamically evolved and flow-dependent nonlinear perturbations, indicating the most unstable modes of the underlying flow. Especially over smaller areas, however, BVs with different initial seeds may to some extent be constrained to a small subspace, missing potential forecast error growth along other unstable perturbation directions.

In this paper, the authors study the nonlinear local Lyapunov vectors (NLLVs) that are designed to capture an orthogonal basis spanning the most unstable perturbation subspace, thus potentially ameliorating the limitation of BVs. The NLLVs are theoretically related to the linear Lyapunov vectors (LVs), which also form an orthogonal basis. Like BVs, NLLVs are generated by dynamically evolving perturbations with a full nonlinear model. In simulated forecast experiments, a set of mutually orthogonal NLLVs show an advantage in predicting the structure of forecast error growth when compared to using a set of BVs that are not fully independent. NLLVs are also found to have a higher local dimension, enabling them to better capture localized instabilities, leading to increased ensemble spread.

1. Introduction

Because of the chaotic nature of the atmosphere, numerical weather prediction (NWP) will inevitably diverge from the evolution of the true state of the atmosphere, limiting predictability (Lorenz 1963a,b; Ruelle and Takens 1971; Li and Chou 1997). Predictability research explores instabilities of the system that are responsible, along with model errors for the fast growth of forecast errors. Understanding the growth of unstable errors is critical to improvements in NWP. For example, the ingestion of supplementary observations over carefully chosen dynamically unstable regions can reduce analysis and ensuing forecast uncertainties (Lorenz and Emanuel 1998; Bishop and Toth 1999; Bishop et al. 2001; Mu 2013), fast-growing perturbations (perts) can be used to define background forecast error covariance in data assimilation (DA) algorithms (Trevisan and Uboldi 2004; Uboldi et al. 2005), and dynamically conditioned growing perturbations are used in ensemble forecasting to capture analysis–forecast error development (e.g., Toth and Kalnay 1993, 1997; Molteni and Palmer 1993; Molteni et al. 1996).

Corresponding author: Dr. Jianping Li, ljp@bnu.edu.cn

DOI: 10.1175/JAS-D-17-0266.1

Various methods have been proposed to characterize the instabilities of chaotic systems, including the atmosphere. The leading Lyapunov vector (LV) defines the fastest-growing linear perturbation at a certain time, toward which any infinitesimal perturbation will converge after long time evolution (Kalnay 2003). Other fast-growing perturbation directions can be derived by evolving a set of perturbations using the tangent linear model of a system and conducting periodic orthogonalization (Benettin et al. 1980; Wolf et al. 1985; Kalnay 2003). Bred vectors (BVs; Toth and Kalnay 1993) sample the subspace of fastest-growing finite-amplitude perturbations. They are captured by following the periodically rescaled evolution of perturbations between two nonlinear forecasts. As such, BVs can be considered as the nonlinear extension of the leading LV (Toth and Kalnay 1997; Kalnay et al. 2002). Perturbation size can be controlled by the choice of the rescaling period and amplitude. In complex dynamical systems, BVs are associated with instabilities characterized by the fastest perturbation growth in the selected amplitude range (Toth and Kalnay 1997). For example, at amplitudes in the range of error variance of today's NWP initial conditions (i.e., analysis fields), BVs strongly project onto baroclinic instabilities (Toth and Kalnay 1997; Corazza et al. 2003; Wei and Frederiksen 2004), while convective instabilities dominate at much lower perturbation amplitudes (Toth and Kalnay 1997). The BV approach has been widely applied in NWP because of its conceptual simplicity and computational efficiency.

By definition, singular vectors (SVs) are the linearly fastest-growing perturbations over a specified time period, measured with a specific preselected norm (Molteni and Palmer 1993; Molteni et al. 1996). Unlike LVs that represent temporally sustainable behavior, SVs explore transitional behavior (Szunyogh et al. 1997). Their growth exhibits apparent ''super Lyapunov'' growth because of fast-decaying, trailing LVs that at initial time make part of the growing perturbation structure ''invisible'' through the chosen norm (Toth et al. 1999). Hence, growth over the selected period, only when evaluated via the chosen norm, appears very large. Despite their more specific definition and significantly higher computational costs, SVs have been widely used in predictability studies. Mu et al. (2003) proposed a nonlinear extension of the SVs, called conditional nonlinear optimal perturbations (CNOPs). CNOPs have been successfully applied to analyze regions of sensitive error growth (Duan et al. 2004; Mu et al. 2007; Mu et al. 2009; Zhang et al. 2015). Beyond these basic and widely used tools, a variety of other methods has also been proposed to study instabilities and associated predictability, both from theoretical and more practical perspectives.

As for BVs, when multiple vectors (each started with a different initial seed perturbation) are computed, they evolve into globally quasi-independent and similarly fast-growing perturbations (Toth and Kalnay 1997). This is partly due to stochastic effects arising from nonlinear perturbation evolution. Previous studies also found, however, that multiple independently run BV perturbations regionally collapse into a small subspace in areas of high growth (Toth and Kalnay 1997). This may result in an underestimation of the diversity in plausible forecast error patterns (Wang and Bishop 2003; Bowler 2006), especially in regions with strong instabilities (Patil et al. 2001, 2003). One may theorize that the small subspace of the fastest-growing perturbations sampled by the BVs may not capture all potential error patterns in complex dynamical systems.

To mitigate the potential collapse of independently run BV perturbations into an undesirably small subspace, various forms of orthogonalization of the perturbations have been explored. For example, Annan (2004) derived the fastest-growing perturbation by comparing the growth rates of orthogonal BVs.[1] Keller et al. (2010) made singular-value decomposition to BVs to obtain the independent dominated unstable perturbations. Primo et al. (2008) introduced a new logarithm BV to increase the diversity of the ensemble. Balci et al. (2012) used the size of the largest member of BVs as the uniform scaling of the ensemble. The ensemble transform Kalman filter (ETKF; Bishop et al. 2001; Wei et al. 2006) or the ensemble transform with rescaling (ETR; Wei et al. 2008) transform BVs to quasi-orthogonalized perturbations. Feng et al. (2014, 2016) proposed a method analogous to ETR called the nonlinear local Lyapunov vectors (NLLVs). Although both the ETR and the NLLV methods ''breed'' the perturbations to the unstable directions during the forecast phase, they transform the subspace of perturbations in different ways. The former increases the diversity of perturbations by multiplying a transformation matrix to the perturbation matrix, while the NLLV scheme uses the Gram–Schmidt reorthonormalization (GSR) to orthogonalize the perturbations in cycles, separating independent perturbation directions with different growth rates.

NLLVs are related to the spectrum of nonlinear local Lyapunov exponents (NLLEs). Traditional or linear Lyapunov exponents (LEs) measure the expansion or

[1] Note that the differences between the method in Annan (2004) and the NLLV scheme is that the former orthogonalizes BVs and compares their growth rates mainly to obtain the fastest-growing perturbation rather than the overall fastest unstable perturbation subspace. Meanwhile, the perturbations in the final breeding cycle are not orthogonalized and thereby are not strictly independent.

shrinking of infinitesimal perturbations averaged over the entire phase-space domain of a dynamical system (i.e., the LVs; Oseledec 1968). Hence, LEs characterize only the global and linear behavior of systems. Some subsequent studies expanded the practical applications of LEs by developing concepts for finite evolution time (Abarbanel et al. 1991) or finite-size LEs (Aurell et al. 1997). In contrast, NLLEs are introduced to measure the growth rate of finite-size perturbation along different perturbation directions at a specific initial state within finite evolution time (Ding and Li 2007; Li and Ding 2011). The leading NLLE can be used to estimate the largest LE by taking their temporal mean (i.e., over the entire attractor) if sufficiently small initial errors are used (Chen et al. 2006; Ding and Li 2007; Li and Ding 2011, 2015), whereas NLLEs averaged over different initial perturbations for any specific state offer a way to quantify local predictability (Ding et al. 2008). Complex dynamical systems are characterized by amplification rates that vary with perturbation directions (Li and Wang 2008), yielding a spectrum of NLLEs. The largest NLLE characterizes the exponential growth rate of the leading NLLV (LNLLV). The other exponents can be calculated by introducing the subsequent independent NLLVs. Theoretically, the BVs are an extension of the leading LV, while the NLLVs are inherited from the leading LV and other orthogonal LVs in a nonlinear framework.

Previous simple model studies (Feng et al. 2014, 2016) limited their analysis to the properties of the global NLLV perturbations, leaving the spatial structure and other local properties of NLLVs unexplored. The NLLVs are generated through the breeding technique like the BVs. During the breeding, the stable perturbations will diminish, while the unstable perturbations will amplify and become dominated, making the perturbation patterns (i.e., the BVs and the LNLLV) manifest the physical instabilities in the model (Greybush et al. 2013). The other NLLVs are similar to the BVs but reveal instabilities on different directions. This paper will compare how BVs and their enhanced counterpart, NLLVs, perform in numerical experiments in estimating the structure of forecast error amplification while studying localized instabilities as the underlying mechanism. Such a study will provide a foundation for the application of NLLVs in the identification of the sensitive regions with fast error growth and the generation of initial ensemble perturbations for capturing case-dependent analysis errors.

The rest of the paper is structured as follows. Section 2 introduces the numerical model and the methods associated with BVs and the NLLVs used in this paper. The flow of the experimental design is described in section 3. Results and their analysis are found in section 4, while section 5 offers some conclusions and a discussion.

2. Model and methods

a. Model

The numerical model used in this paper is a T21L3 quasi-geographic (QG) model (Marshall and Molteni 1993). This is a global spectral model with horizontal resolution of T21 (64 × 32) and three vertical levels corresponding to the 200-, 500-, and 800-hPa pressure levels. The model uses a perpetual forcing to reproduce the northern winter climatology. Although the QG model with 1449 degrees of freedom (Vannitsem and Nicolis 1997) is relatively simple compared to NWP models, it is well suited for this study since it can successfully simulate the mean large-scale midlatitudes flow, reflecting the mechanism of baroclinic instabilities important in forecast error growth (Goodman and Marshall 2002). In other words, the baroclinic instability could be the main origin of the development of errors and perturbations in this model. The study area is focused on the mid- and high latitudes of the Northern Hemisphere (20°–85°N), and the variable of interest is the geopotential height (GPH) at 500 hPa.

b. Computation of bred vectors

Each BV is generated through similar, independently run breeding processes, in each of which the differences between two nonlinear model integrations are evolved and rescaled periodically:

1) Consider a series of successive reference states $\mathbf{x}_{-K\Delta t}, \mathbf{x}_{-(K-1)\Delta t}, \ldots, \mathbf{x}_0$, where Δt is the length of breeding cycle and K is the number of cycles. The negative indices represent the breeding period. Superpose a small perturbation $\boldsymbol{\delta}_{-K\Delta t}$ of size A (in an L_2 norm) on $\mathbf{x}_{-K\Delta t}$ and then integrate the perturbed state $\mathbf{x}'_{-K\Delta t}$ with the full nonlinear model for Δt interval to acquire the forecast state $f(\mathbf{x}'_{-K\Delta t}, \Delta t)$. When a breeding cycle is started, $\boldsymbol{\delta}_{-K\Delta t}$ is chosen to be a random perturbation.
2) Let $\boldsymbol{\delta}'_{-(K-1)\Delta t}$ denote the difference between the perturbed forecast $f(\mathbf{x}'_{-K\Delta t}, \Delta t)$ and the reference $\mathbf{x}_{-(K-1)\Delta t}$; $\boldsymbol{\delta}'_{-(K-1)\Delta t}$ is then rescaled to the size A of the initial perturbation, and the updated perturbation is expressed as

$$\boldsymbol{\delta}_{-(K-1)\Delta t} = \boldsymbol{\delta}'_{-(K-1)\Delta t} A / \|\boldsymbol{\delta}'_{-(K-1)\Delta t}\|, \qquad (1)$$

   where $\|\cdot\|$ represents the norm of a vector.
3) Superpose the rescaled perturbation $\boldsymbol{\delta}_{-(K-1)\Delta t}$ on the subsequent reference $\mathbf{x}_{-(K-1)\Delta t}$ and repeat steps 1 and 2 for K cycles to $\mathbf{x}_0$ to derive the BVs.

Through the dynamical evolution, the decaying, neutral, and slower-growing components in the initial random perturbations will be gradually eliminated, leading to the projection of BVs onto the fastest-growing directions. Multiple BVs can be obtained by simply selecting different initial random seeds. The BVs have dominant projections on the leading LVs and span the small subspace of the fastest-growing directions.

c. *Computation of nonlinear local Lyapunov vectors*

The NLLVs are related to the BVs, and computed as follows:

1) Consider the same series of reference states $\mathbf{x}_{-K\Delta t}$, $\mathbf{x}_{-(K-1)\Delta t}, \ldots, \mathbf{x}_0$ as in section 2b. Superpose a group of M different perturbations $\boldsymbol{\delta}_{1,-K\Delta t}, \boldsymbol{\delta}_{2,-K\Delta t}, \ldots, \boldsymbol{\delta}_{M,-K\Delta t}$ with the same size A on the basic state $\mathbf{x}_{-K\cdot\Delta t}$ and integrate the individual perturbed states $\mathbf{x}'_{1,-K\Delta t}, \mathbf{x}'_{2,-K\Delta t}, \ldots, \mathbf{x}'_{M,-K\Delta t}$ with the full nonlinear model for Δt interval to acquire their respective forecast states $f(\mathbf{x}'_{1,-K\Delta t}, \Delta t)$, $f(\mathbf{x}'_{2,-K\Delta t}, \Delta t), \ldots, f(\mathbf{x}'_{M,-K\Delta t}, \Delta t)$. Again, in the first cycle of the NLLV algorithm, nonidentical initial perturbations are chosen arbitrarily.
2) The differences between the perturbed forecasts and the references at the same valid time $-(K-1)\Delta t$ are denoted by $\boldsymbol{\delta}'_{1,-(K-1)\Delta t}, \boldsymbol{\delta}'_{2,-(K-1)\Delta t}, \ldots, \boldsymbol{\delta}'_{M,-(K-1)\Delta t}$. Without changing the direction of the first perturbation $\boldsymbol{\delta}'_{1,-(K-1)\Delta t}$, we orthogonalize the other perturbations successively using the GSR algorithm[2] (Wolf et al. 1985; Li and Wang 2008) and then rescale all of them to size A as in Eq. (1) to derive the following perturbations: $\boldsymbol{\delta}_{1,-(K-1)\Delta t}, \boldsymbol{\delta}_{2,-(K-1)\Delta t}, \ldots, \boldsymbol{\delta}_{M,-(K-1)\Delta t}$.
3) Superpose the new perturbations on the reference state and repeat steps 1 and 2 in a cyclical fashion to obtain the NLLVs.

The difference between BVs and NLLVs is that while the former vectors are evolved independently, NLLVs are periodically orthogonalized through the GSR method. Specifically, BVs are random samples of the fastest-growing perturbation, leading to uncertain performance in spanning the subspace of unstable perturbations. In comparison, the orthogonalization enables NLLVs to selectively capture multiple independent fast-growing perturbations and span the unstable subspace with fewer sampling fluctuations. Therefore, NLLVs give a more systematic description of the subspace of the fast-growing perturbation directions than BVs.

3. Experimental configuration

It has been demonstrated that the BVs rescaled to amplitudes corresponding to midlatitude analysis-error variance are dominated by baroclinic instabilities, which mainly determine the short-term error growth of synoptic-scale forecasts (Toth and Kalnay 1997). Since the NLLVs are generated using the same rescaling factor and length of evolution cycle as the BVs, the LNLLV has exactly the same properties as the BVs. Whether the additional, lower-rank NLLVs are also associated with the dynamical instabilities and how they describe such instabilities compared to the BVs are the main issues to be analyzed and clarified in this paper.

The schematic of the experimental setup was shown in Fig. 1. Simulating a realistic situation, a long series of successive analysis states generated with a 12-h-cycle ensemble Kalman filter (EnKF) scheme are used as a representation of the basic flow for the computation of BV and NLLV perturbations (see Fig. 1b) and also as reference states that the forecasts are compared with (see Fig. 1a). Each analysis state is the average of 200 EnKF analysis ensemble. The details of the EnKF procedures are described in appendix A. The practical error growth of EnKF ensemble forecasts against analyses will be used to verify the accuracy of BV and NLLV perturbations in capturing the flow instabilities. As a benchmark, the growth of random errors will also be used in one set of experiments as an alternative to the more realistic ENKF-produced analysis errors. The gridpoint initial random errors are drawn from a Gaussian distribution with a zero mean and a standard deviation (SD) equal to 5% of the climatological SD of the QG model, which are then globally rescaled to the same size (7.5, 5, and 3.75 m in an L_2 norm at 200, 500, and 800 hPa, respectively) as the BV and NLLV perturbations.

The same number (10) of NLLVs and BVs are generated for a contiguous period as described in section 2, with a 12-h rescaling cycle and global rescaling amplitudes of 7.5, 5, and 3.75 m (in an L_2 norm) at 200, 500, and 800 hPa, respectively, corresponding to about 5% of the global-mean climatic variability at each level. The value of 5% was selected because BVs rescaled with 1%–10% of the natural variability are found

[2] The reordering of perturbations according to their growth rates before the application of GSR in Feng et al. (2014) made no significant changes in the performance of the MAP–SDEG correlation compared to the direct GSR to the perturbations without reordering and therefore was not applied here. It could be the much flatter Lyapunov spectrum (Vannitsem and Nicolis 1997) of the growing subspace in the QG model relative to the three-variable Lorenz model used by Feng et al. (2014) that weakens the effect of the reordering on capturing the unstable subspace.

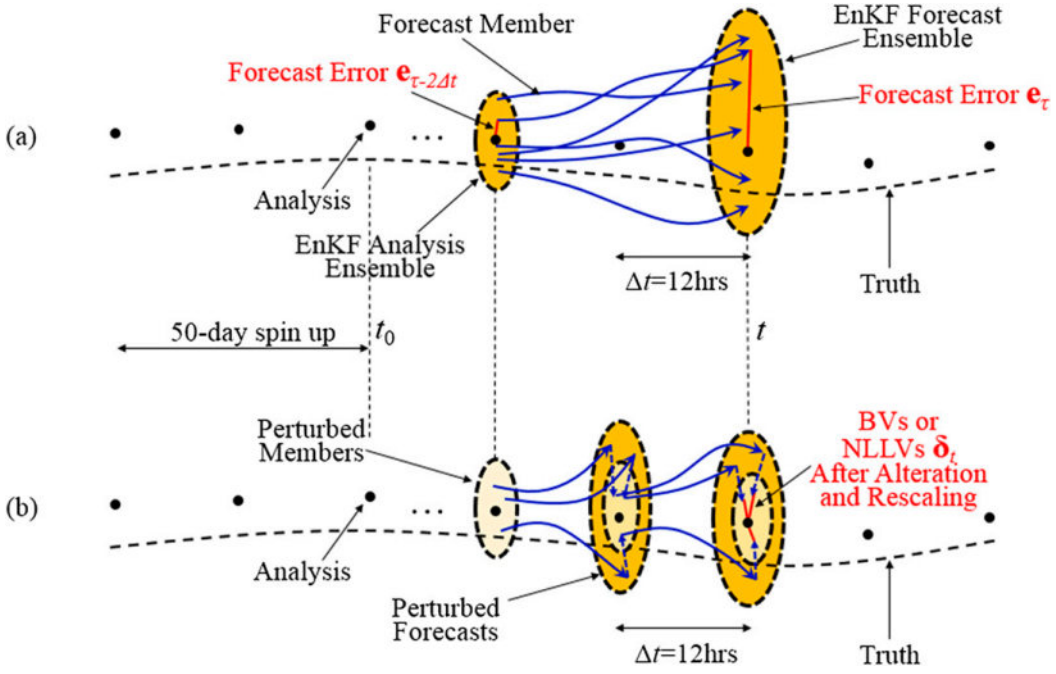

FIG. 1. Schematics of (a) the computation of forecast errors and (b) the generation of BVs and NLLVs.

closely associated with extratropical baroclinic instability (Toth and Kalnay 1997). To diminish the effect of the initial random components in BVs and NLLVs, the first 50 days of cycling were discarded, after which we study 90 consecutive cases at a 1-day interval (one season).

We will use the correlation between two metrics, that is, the mean absolute perturbation (MAP) and the spatial distribution of error growth (SDEG), to evaluate the relative performance of BVs and NLLVs. Previous studies have found the BV perturbations and the forecast errors have some similar structures, especially in some local regions with fast error growth, although they may have different signs (Toth and Kalnay 1997; Corazza et al. 2003; Newman et al. 2004; Yang et al. 2009). MAP and SDEG are defined as somewhat modified forms of the generally used dynamical perturbations and forecast errors, respectively. Since our aim here is to quantify the correlation relationship between the fields of perturbations and error growth, the absolute perturbations instead of the original ones are used (i.e., the MAP) to estimate the instabilities. As a reference for evaluating the instabilities, the error growth (i.e., the SDEG) instead of the forecast error is used since the former is more directly related to instabilities and was found to have higher spatial correlation with MAP of both BVs and NLLVs than the forecast error amplitudes in our study (not shown). The MAP of BVs and NLLVs at valid time t denoted by $\mathbf{u}_t$ are calculated by

$$\mathbf{u}_t = (\mathbf{p}_{t,1} + \mathbf{p}_{t,2} + \cdots + \mathbf{p}_{t,M})/M, \tag{2}$$

where $\mathbf{p}_{t,i} = \mathrm{abs}(\boldsymbol{\delta}_{t,i})$ ($i = 1, 2, \ldots, M$), and $\boldsymbol{\delta}_{t,i}$ is the ith BV or NLLV in order at time t (red solid lines in Fig. 1b), and abs(·) means all gridpoint perturbations converted to absolute values. Generally, one randomly selected BV is already sufficient to indicate the instabilities because of their similarities (Corazza et al. 2003), though the use of a larger sample may reduce sampling fluctuations. Here, the same number of BVs as the NLLVs is used for a fair comparison.

The SDEG at valid time t denoted by $\mathbf{d}_t$ is simply measured as the increment of absolute errors in 1 day, namely

$$\mathbf{d}_t = \mathrm{abs}(\mathbf{e}_{\tau}) - \mathrm{abs}(\mathbf{e}_{\tau-2\Delta t}), \tag{3}$$

where $\mathbf{e}_{\tau}$ and $\mathbf{e}_{\tau-2\Delta t}$ are both forecast error fields valid at time t and 1 day before t, respectively. Specifically, $\mathbf{e}_{\tau} = \mathbf{F}_{\tau} - \mathbf{A}$, $\mathbf{e}_{\tau-2\Delta t} = \mathbf{F}_{\tau-2\Delta t} - \mathbf{A}$, where $\mathbf{F}_{\tau}$ and $\mathbf{F}_{\tau-2\Delta t}$ are the forecasts with lead times τ and $\tau - 2\Delta t$ (Δt = 12 h) from the same initial state and $\mathbf{A}$ is the corresponding analysis field. In the experiment with EnKF-produced analysis errors, the forecasts are initiated from the EnKF analysis members, and SDEG is computed for the first day (τ = 24 h), while in the experiment with random initial errors, forecasts are started from randomly perturbed conditions, and SDEG is calculated from 2 to 3 days (τ = 72 h) after an initial spinup. The

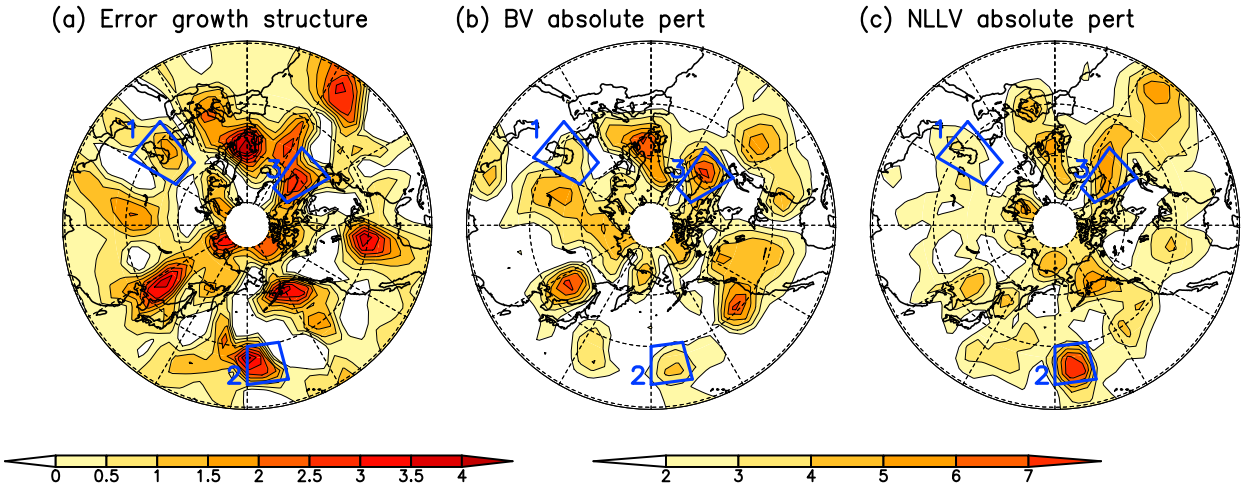

FIG. 2. (a) The SDEG of random initial errors within 1 day and the MAPs generated by combining five (b) BVs and (c) NLLVs at the same valid time in one randomly selected case. The spatial correlations between (a) and (b) and between (a) and (c) are 0.37 and 0.54, respectively.

SDEG investigated in the above two scenarios are within the approximately linear error growth stage. To reduce sampling noise, for each case, SDEG is computed by averaging the error growth in 200 different ensemble forecasts initiated at the same time. We will use the pattern correlation between MAP and SDEG at the same valid time t as an indicator of how well a type of perturbation (BVs or NLLVs in our case) captures the instability of flow and the behavior of errors.

4. Results

a. Growth of random perturbations

In the first experiment, forecasts are initialized with arbitrarily generated initial errors superposed on EnKF analysis to assess the efficiency of BV and NLLV perturbations to describe forecast error growth. To reduce the effect of noise in the random initial errors, SDEG is computed between day-3 and day-2 forecasts instead of day-1 and day-0 conditions (but valid at the same time for which the BVs and NLLVs are generated).

Figure 2 shows the SDEG (Fig. 2a) and the MAPs captured by five randomly selected BVs (Fig. 2b) and the first five NLLVs in a randomly selected case (case 1; Fig. 2c). As seen from Fig. 2a, SDEG of 500-hPa GPH exhibits large-scale zonally oriented patterns possibly associated with the eddy activity concentrated in storm-track regions (Buizza and Palmer 1995; Vannitsem and Nicolis 1998), which suggests that the baroclinic instabilities could be the source of the major forecast uncertainties. The MAPs in Figs. 2b and 2c also appear to follow wavelike patterns. Many areas of strong instability, indicated by local BV MAP maxima, correspond with areas of fast forecast error growth; see as examples the highlighted areas over 1) the Caspian Sea, 2) the mid-latitude central Pacific Ocean, and 3) southern Greenland. It is noteworthy that the NLLV MAP is also capable of catching these unstable regions as shown in Fig. 2c. Moreover, the NLLV MAP better specifies the relative strength of the forecast error growth over these three regions (region 2 > region 3 > region 1). Although the BV MAP exhibits the strength of some local error growth more accurately than the NLLVs, like East Asia, the latter (0.54) has an overall higher pattern correlation with the error growth structure than the former (0.37). The results indicate that in addition to the LNLLV, the other leading NLLVs may also be related to the dynamical instabilities. Furthermore, a set of the leading NLLVs appear to capture more robustly the dynamics underlying forecast error growth than a similarly sized set of BVs.

To obtain statistically reliable results, for this case, we repeated the generation of BVs and NLLVs 100 times, using different initial random seeds. Figure 3 shows their comparison of the SDEG–MAP correlation in each sample. In 92 samples, the NLLV scheme has higher correlation than the BV scheme. The NLLVs have higher sample-mean correlation (0.52) and lower SD (0.034) than those of the BVs (0.44 and 0.039) and the difference between their mean values is statistically significant ($P < 0.01$), which demonstrate the more stable performance of the NLLV MAPs in revealing the SDEG compared to the BVs.

Figure 4a compares the pattern correlation between the SDEG and the MAPs of the BV (black) and NLLV (red) schemes averaged over all 90 cases as a function of the number of perturbations used. When only one

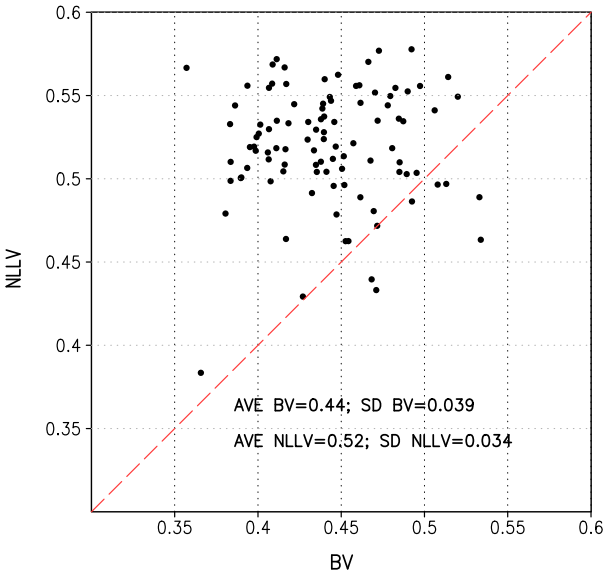

FIG. 3. The spatial correlation between the SDEG of random initial errors and the MAPs derived from five BVs and NLLVs in the same case as Fig. 1 but repeated for 100 times with BVs and NLLVs generated from different initial random seeds. The mean correlations and the SD of the 100 samples are 0.44 and 0.039 for the BV scheme and are 0.52 and 0.034 for the NLLV scheme. It has 92 (92%) cases where the NLLVs have higher correlation than the BVs.

perturbation is used, since the leading NLLV and any BV, by definition, are generated the same way, the results are virtually identical. With an increase in the number of perturbations used, both the BVs and NLLVs display a better performance in terms of explaining the spatial distribution of error growth and exceed the 0.01 significance level,[3] though beyond five perturbations, their performance levels off. However, NLLVs outperform BVs, and ever more so with larger number of perturbations. Figure 4b presents the percentage of cases in which the NLLVs gained a higher SDEG–MAP correlation than the BVs as a function of number of used perturbations. Except for the same performance with a single perturbation, in the majority of cases, NLLVs perform better, in even more than 80% cases from numbers 6 to 10. These results indicate that the independent information in a set of NLLVs carry useful information regarding error evolution beyond what the BVs provide.

[3] The score of the 0.01 significance level (close to 0.3) is lower than the generally used value of 0.6 in operational forecasts, because the model effective spatial degree of freedom and the verified variables (the former is 500-hPa GPH, while the latter is its forecast error growth) are different.

b. *Growth of EnKF ensemble perturbations*

In reality, analysis errors are not random since NWP initial states optimally combine short-range model forecasts with observations. Correspondingly, in a more realistic context, we used EnKF initial ensemble perturbations, usually regarded as reliable estimates of analysis uncertainty, as a proxy for analysis errors when initializing NWP forecasts (i.e., the analysis considered as the "truth"). For each of the 90 cases studied above, SDEG is calculated by averaging the amplification of all 200 EnKF ensemble perturbations.

Figure 5 shows the SDEG (Fig. 5a) and its corresponding BV (Fig. 5b) and NLLV MAPs (Fig. 5c) for the same case as Fig. 2. The areas with positive error growth in Fig. 5a are overall larger than in Fig. 2a because the latter has more transitional behavior of initial errors due to more random noises in analysis errors (Trevisan and Legnani 1995). Similar to the results in Fig. 2, the regions with fast error growth are related to the localized unstable perturbations in both the BV and NLLV modes, and again, the order of the forecast error growth over the regions 1–3 is better simulated by the NLLVs than the BVs. Correspondingly, the NLLV mode (0.52) has higher correlation with the SDEG than with the BV mode (0.27).

The mean SDEG–MAP correlation for all 90 cases as a function of number of perturbations is shown in Fig. 6a. As in Fig. 4a, the correlation increases with the number of perturbations. While the correlation for BVs appear to saturate at a value around 0.4 correlation, the correlation for NLLVs are higher (up to 0.5). We also compared the EnKF analysis ensemble perturbations (differences between the EnKF initial ensemble and their average) with the BVs and NLLVs at the same valid time in terms of estimating SDEG (blue line in Fig. 6a). The correlations between the EnKF analysis ensemble perturbations and SDEG increase with the number of used perturbations but perform overall worse than the BVs and NLLVs. In the DA cycle, the EnKF analysis ensemble perturbations are generated by transforming the EnKF background forecast perturbations, which, like the BVs and NLLVs, point to the directions of instabilities during the forecast phase. However, the ingestion of observations in the DA step, although it improves the accuracy of EnKF initial perturbations in representing the uncertainties in analyses, introduces random noises (or stable components) to the initial perturbations (Toth and Kalnay 1997; Hamill et al. 2002; Peña et al. 2010). The performance of EnKF analysis perturbations in manifesting the instabilities is thus degraded. Figure 6b compares the SDEG–MAP correlation score for the BV and the NLLV methods with different number of perturbations averaged over

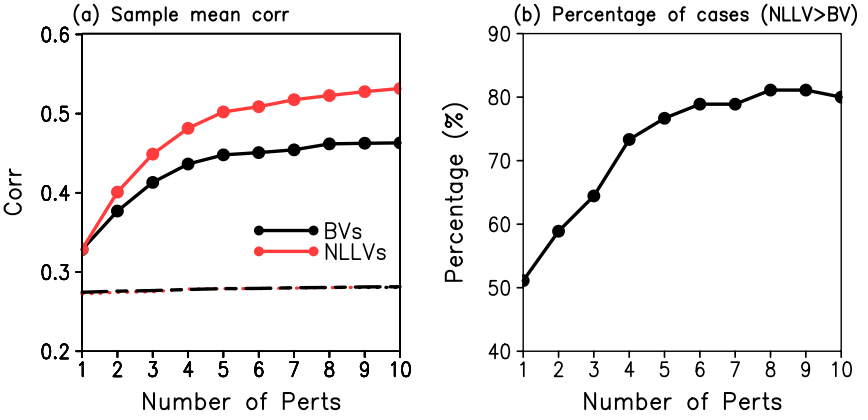

FIG. 4. (a) The spatial correlation between SDEG of random initial errors and MAPs derived from 1 to 10 BVs (black solid line) and NLLVs (red solid line) averaged over all 90 cases as a function of the number of perturbations used. The black and red dashed lines represent their respective 0.01 significance levels for the correlation. (b) The percentage of cases in which the NLLV scheme has higher SDEG–MAP correlation than the BV scheme as a function of the number of perturbations used.

the 90 cases. With EnKF initial errors, NLLVs perform even better, outperforming BVs in close to 90% of the cases with eight or more perturbations (cf. Figs. 6b and 4b with random initial errors).

The difference between NLLV and BV correlation values with SDEG for $M = 5$ perturbations for the 90 individual cases is shown in Fig. 7 (black line). Interestingly, the case-to-case variability in the comparative performance of MAPs in predicting changes in forecast error (SDEG) is closely correlated ($r = 0.83$, significant at the 0.01 level) with the difference in the variance explained in error amplification (SDEG) by the two types of MAPs (red curve in Fig. 7). The latter quantity is defined similarly to the perturbation versus error correlation analysis (PECA) proposed by Wei and Toth (2003). Specifically, if $\mathbf{P}' = (p'_1, p'_2, \ldots, p'_M)$ are the standardized perturbations (with L_2 norm 1) of $\mathbf{p}_1, \mathbf{p}_2, \ldots, \mathbf{p}_M$, where $M = 5$, the projection of the SDEG $\mathbf{d}$ on the subspace of perturbations $\mathbf{p}_1, \mathbf{p}_2, \ldots, \mathbf{p}_M$ can be derived by $\mathbf{q} = \mathbf{P}'\mathbf{P}'^{\mathrm{T}}\mathbf{d}$, where the superscript T represents the transpose of a matrix. The variance of $\mathbf{d}$ projected onto the ensemble perturbations (i.e., explained variance) is then calculated by the square of the correlation between $\mathbf{d}$ and $\mathbf{q}$. It is also notable that while BVs outperform NLLVs in 18 out of the 90 cases in terms of the correlation metrics, they do so only in 14 cases when compared in terms of explained error variance. These results once again demonstrate the advantage of

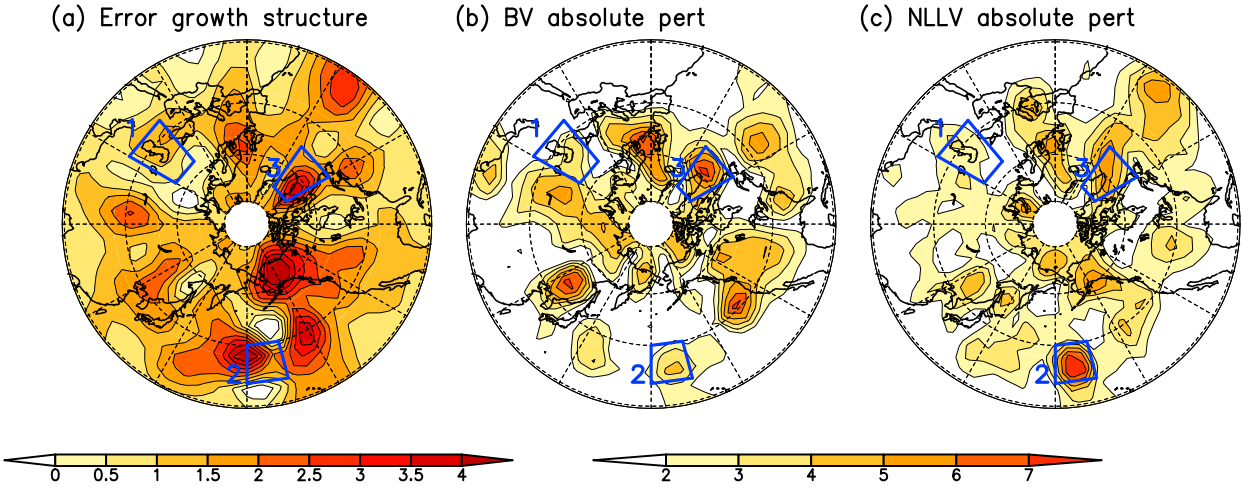

FIG. 5. As in Fig. 2, but the EnKF ensemble perturbations are used as initial errors to estimate the SDEG. The spatial correlations between (a) and (b) and between (a) and (c) are 0.27 and 0.52, respectively.

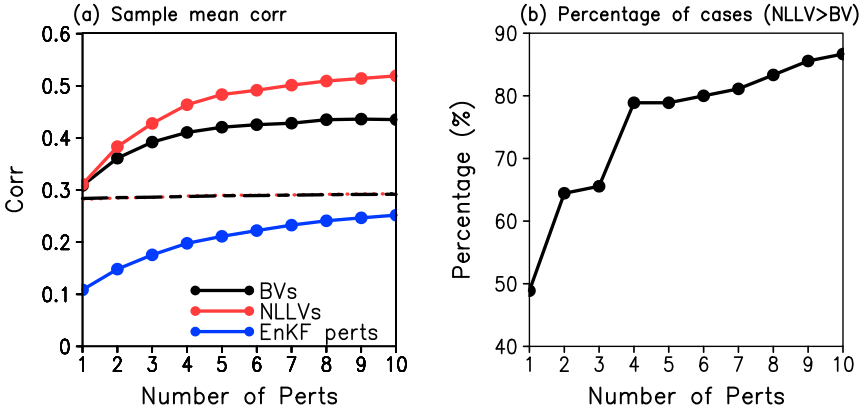

FIG. 6. As in Fig. 4, but the EnKF analysis ensemble perturbations are used as initial errors to estimate the SDEG. The performance of MAP derived from EnKF analysis ensemble perturbations is also shown (blue line in Fig. 6a).

NLLVs over the BV MAPs in imitating the SDEG now in a more realistic experimental environment, with EnKF initial errors.

c. *Independence of NLLV and BV perturbations*

The higher variance of SDEG that NLLVs can explain as compared to BVs may be related to the larger subspace of growing perturbations spanned by the NLLVs because of their orthogonality at the initial time. Other things being equal, more uncorrelated and independent growing perturbations are more likely to capture the comprehensive properties of instabilities manifested in SDEG. Here, the explained variance of the eigenvectors of the covariance matrix of ensemble perturbations is used to evaluate the dependence in a set of perturbations. Specifically, for ensemble perturbations $\mathbf{\Delta} = (\boldsymbol{\delta}_1, \boldsymbol{\delta}_2, \ldots, \boldsymbol{\delta}_M)$, the covariance matrix can be written as $\mathbf{R} = \mathbf{\Delta}\mathbf{\Delta}^{\mathrm{T}}$. We use an empirical orthogonal function analysis to solve for eigenvalues $\lambda_1, \lambda_2, \ldots, \lambda_M$ of $\mathbf{R}$ to calculate the explained variances ρ_i as $\rho_i = \lambda_i \Big/ \left(\sum_{i=1}^{M} \lambda_i\right)$.

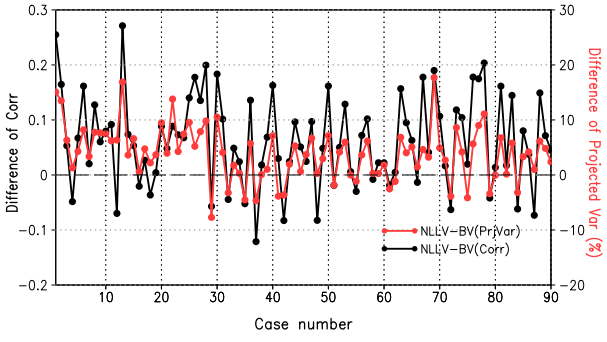

FIG. 7. The differences (black) between the SDEG–MAP correlations of the BV and NLLV schemes and the differences (red) between the percentages of the projected variances of SDEG on the subspace of the BV and NLLV absolute perturbations. Their correlation over all 90 cases is 0.83, which is significant at 0.01 level.

As seen from Fig. 8, the first five NLLVs exhibit a closer to uniform distribution[4] of explained variance as compared to five randomly chosen BVs[5] averaged over all 90 cases. In other words, NLLVs span the local phase space of growing directions with more diverse perturbations than do the BVs. This larger diversity makes NLLV MAP a better predictor of changes in analysis-error magnitude that is dynamically driven by multiple growing instabilities compared to the more correlated BVs, as revealed in sections 5a and 5b.

d. *Local dimension of BVs and NLLVs*

Patil et al. (2001, 2003) proposed an algorithm for the calculation of the local dimension to assess the dependence of perturbations over local regions. Moreover, they found that the local dimensions of BVs are related to the dynamical instabilities of error development. Specifically, over the regions with stronger instability, the perturbations exhibit more consistent tendency to concentrate and thus have more converged directions and lower local dimensions. The impact of the global orthogonalization of NLLVs on the characteristics of local perturbations can be investigated by comparing the local dimensions to those of BVs. Using Patil et al.'s (2001) algorithm (see more details in

[4] Note that since they are globally orthogonalized, over the Northern Hemisphere, the NLLV perturbations do not present a totally uniform distribution of explained variances.

[5] The original BV and NLLV perturbations with signs are used here instead of the absolute perturbations since the latter are in comparison more correlated overall; however, they have a similar relative performance of the dependence.

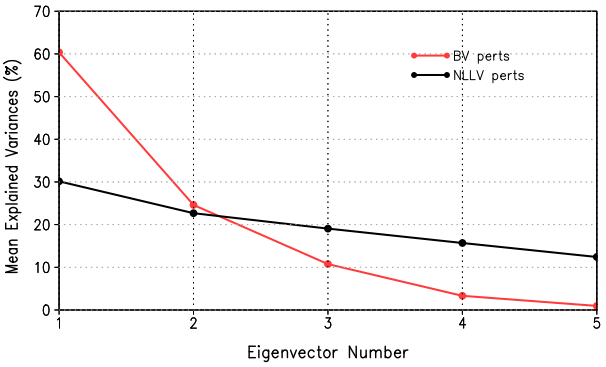

FIG. 8. The explained variances of the eigenvectors of the covariance matrix of five BV and NLLV perturbations over the Northern Hemisphere averaged over all 90 cases.

appendix B), here, we compare the dimension of five local BV and NLLV perturbations in 5 × 5 grid boxes centered at each grid point at 500 hPa.

Figure 9 shows a comparison of the distribution of the local dimensions of five BVs and NLLVs in case 1 (the same case as in Figs. 2 and 5). As seen in Fig. 9a, the local dimensionality of BVs and NLLVs are spatially weakly correlated at the 0.47 level. This is a typical example as the mean of the correlations taken over all 90 cases is 0.45. At the majority of grid points, however, the local NLLV dimension is higher than the local BV dimension (see Fig. 9b). This is true for the other cases as well. As seen in Fig. 10, the number of cases with higher NLLV than BV dimension exceeds 90% over three-fourths of the domain considered. The higher NLLV dimension is due to the global orthogonalization of the NLLVs and is an indication of more independent perturbations in the NLLVs.

Applying a method similar to that used by Toth and Kalnay (1997; see their Fig. 4 and Table 1), we investigate the difference between how individual BVs and NLLVs reflect regional instabilities. In particular, Table 1 tabulates the presence or lack of a local maximum or minimum in five BVs and NLLVs (Fig. 11) over selected regions of fast error growth (see areas A, B, C, and D).

The results in Fig. 11 and Table 1 confirm Toth and Kalnay's (1997) finding that in areas of fast perturbation/error growth, independently cycled BVs reproduce the nonlinearly fastest-growing perturbations and that these regional patterns are combined with arbitrary signs in individual global BVs. BVs naturally combine perturbations from regions with the strongest (i.e., fastest-growing perturbations) and less-strong instabilities, offering a sampling of the fastest-growing perturbation from each unstable region, with random signs. Of the 20 cases (4 selected regions times 5 BVs), only in 2 cases did the BVs have no pronounced local perturbation. This is in contrast with 11 such cases for the NLLVs. The orthogonalization of NLLVs separates perturbations according to their growth rates. Given the strength of instabilities supporting regional perturbation growth varies from region to region, the NLLV procedure also has a geographically selective effect on the vectors: in case 1 studied here, the first two NLLVs, for example, tend to peak in areas C and D, while the lower-ranked perturbations frequent areas A and B. In this respect, NLLVs like linear LLVs and SVs that, because of the simpler linear dynamics, are even more clearly separated geographically (Buizza and Palmer 1995). These results suggest that to simulate the uncertainties of local analysis errors, individual NLLVs, like SVs (Molteni et al. 1996), should not be used directly as ensemble perturbations but rather in a linear combination with other NLLVs. Additionally, the growing components in analysis errors may be randomly located in the unstable subspace spanned by NLLVs and thus should be better sampled by the linear combination of NLLVs.

5. Discussion and conclusions

The abilities of bred vectors (BVs) and nonlinear local Lyapunov vectors (NLLVs) to predict forecast error growth is compared. Both BVs and NLLVs are generated by cycling nonlinear perturbations along a real or proxy trajectory of a system, the difference being that the NLLV procedure involves the periodic application of a Gram–Schmidt orthogonalization step. With such a step, the spectrum of leading NLLVs contains the fastest-growing nonlinear perturbation at a given perturbation amplitude and a set of subsequent perturbations with the fastest growth orthogonal to previous elements. When the performance of the first few NLLVs and a similarly sized set of randomly chosen BVs are compared, we find that NLLVs can better predict the spatial structure of forecast error growth.

The result is closely related to the interdependence between BV or NLLV perturbations. Generally, the growing components of analysis errors are randomly located within the subspace spanned by various most unstable perturbations (Buizza et al. 2005), which may be more comprehensively and specifically simulated by independent NLLVs than the same number of BVs.

It is well known that localized structures in BVs with amplitudes characteristic of error variance in today's analyses correspond to dynamical instabilities. In this paper, NLLVs successive to the leading NLLV (or BV) were found to exhibit similar properties. As expected, the local dimension of a set of NLLVs exceeds that of a similarly sized set of BVs, while spatial variations in the two local dimension fields are correlated.

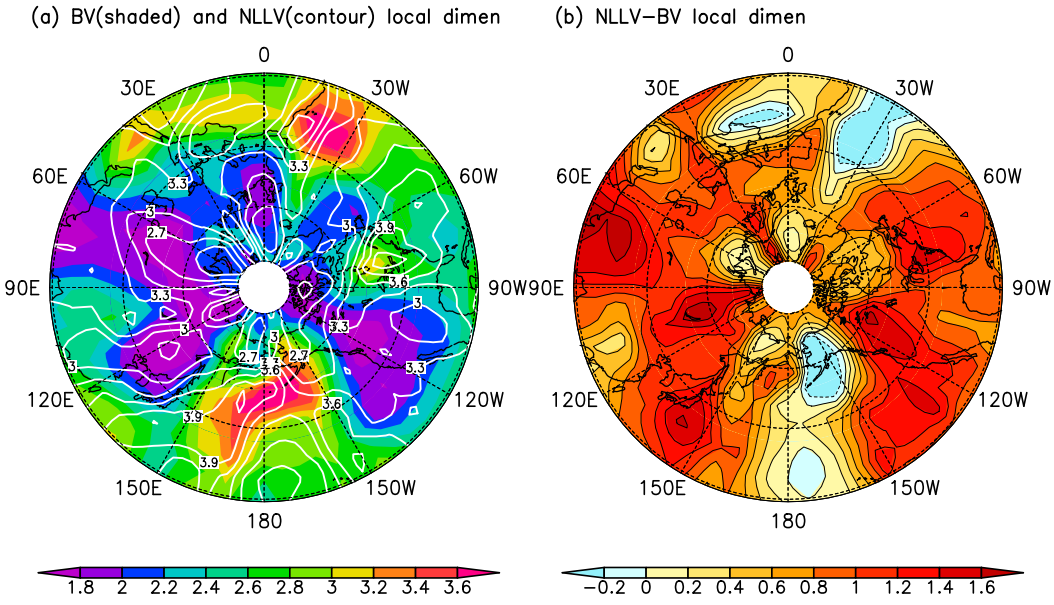

FIG. 9. (a) The distribution of the local dimensions of five BV (shaded) and NLLV (contour) perturbations in the same case as in Figs. 2 and 5. Their spatial correlation is close to 0.47. (b) The difference of the NLLV from the BV local dimension.

The wide-ranging application of BVs in the generation of initial ensemble perturbations is due to their conceptual simplicity, low computational cost, and foremost, their ability to sample the growing modes toward which any perturbation, including the analysis errors, will develop. BVs, however, are not orthogonalized and, therefore, as shown in this study, span a smaller subspace than a similarly sized set of NLLVs, both globally and regionally. This may explain why NLLVs in our experiments outperform BVs in explaining the development of forecast errors. NLLVs, or ensemble transform (ET) perturbations as Wei et al. (2008) call them, were also found to improve forecast skill, presumably because of their more efficient sampling of analysis errors. In potential application to ensemble forecasting, the NLLVs, instead of the global rescaling, can be locally rescaled with an estimated gridded field of analysis-error variance to better represent the uncertainties of analysis errors in local regions. Additionally, the local perturbations of NLLVs are in good agreement with instabilities and thus could be used to identify the regions with potential fast error growth and how errors propagate, which are critical steps before deploying targeted observations. Further studies of the properties and performance of NLLVs with complex NWP models may provide additional insight into atmospheric instabilities and the optimal use of NLLVs in various applications.

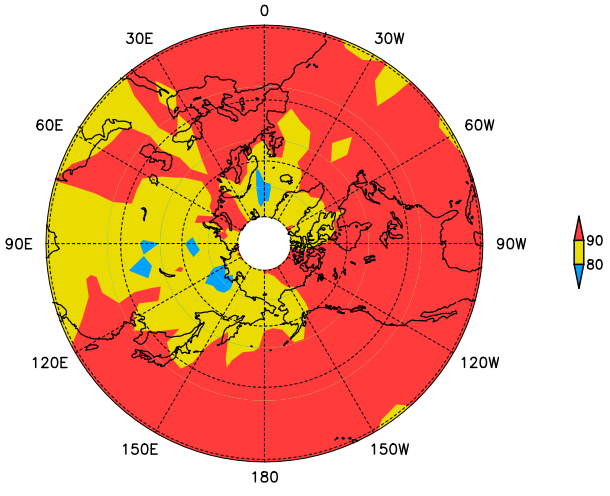

FIG. 10. Percentage of the cases with a higher local dimension for the first five NLLV perturbations than that for the same number of BV perturbations at each grid point.

TABLE 1. Presence (+1 for maximum; −1 for minimum) or lack (0) of local extremum over domains A–D for the five BV and NLLV perturbations in Fig. 11.

		Pert 1	Pert 2	Pert 3	Pert 4	Pert 5	Count
A	BV	−1	+1	0	−1	−1	4
	NLLV	0	0	0	1	0	1
B	BV	+1	−1	−1	+1	+1	5
	NLLV	0	0	1	1	1	3
C	BV	+1	−1	+1	+1	+1	5
	NLLV	1	0	0	0	1	2
D	BV	−1	+1	−1	+1	0	4
	NLLV	1	1	0	0	1	3

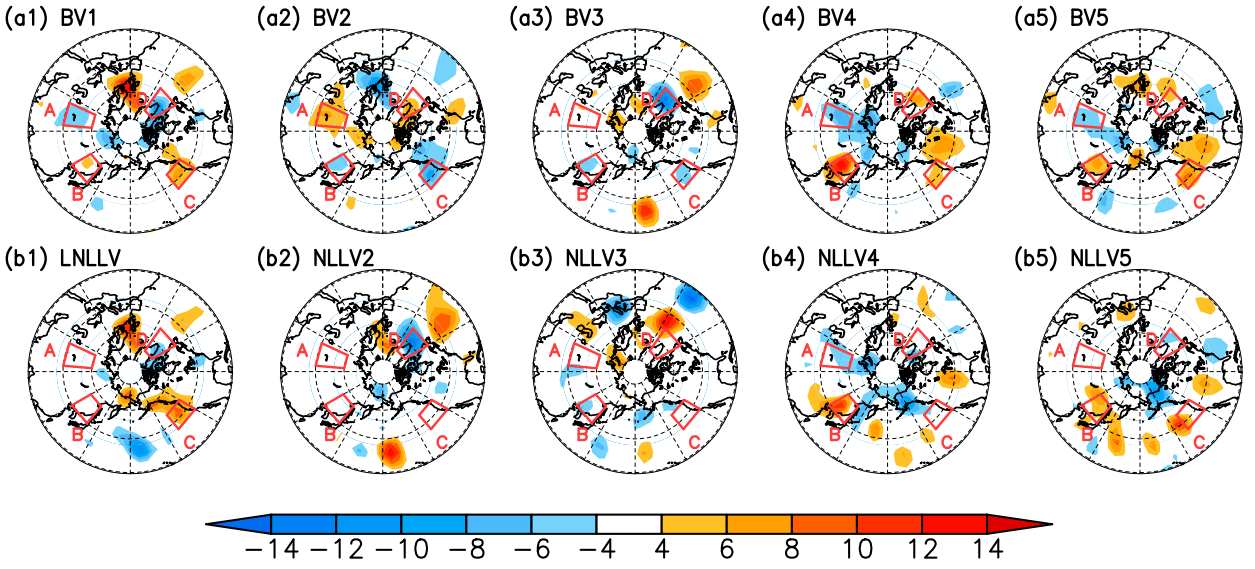

FIG. 11. The spatial patterns of five (a) BV and (b) NLLV perturbations over the Northern Hemisphere (20°–85°N) for case 1 studied in Figs. 2, 5, and 9.

Acknowledgments. We appreciate Drs. John Marshall and Franco Molteni, who kindly provided the numerical model used in this paper. We thank the internal reviewer of GSD, Dr. Guoqing Ge, for the valuable comments. The support of Kevin Kelleher, director of GSD, is gratefully acknowledged. This research was jointly supported by the National Natural Science Foundation of China (NSFC) Grants 41375110 and 41522502, and the SOA International Cooperation Program (GASI-IPOVAI-03).

APPENDIX A

The Ensemble Kalman Filter

We integrate the QG model for an extended time period to obtain a long series of true states $\mathbf{x}^t$. Simulated observations $\mathbf{y}$ are generated by superposing random perturbations $\boldsymbol{\varepsilon}$ on truth:

$$\mathbf{y} = \mathbf{H}\mathbf{x}^t + \boldsymbol{\varepsilon}, \tag{A1}$$

where $\mathbf{H}$ is an operator that projects the states from the model space to the observation space and $\boldsymbol{\varepsilon}$ is the observation errors of GPH (m). Following Houtekamer and Mitchell (1998), $\boldsymbol{\varepsilon}$ are obtained from the covariance matrix:

$$\mathbf{R} = \overline{(\boldsymbol{\varepsilon}_{200}, \boldsymbol{\varepsilon}_{500}, \boldsymbol{\varepsilon}_{800})^{\mathrm{T}}(\boldsymbol{\varepsilon}_{200}, \boldsymbol{\varepsilon}_{500}, \boldsymbol{\varepsilon}_{800})} = \begin{pmatrix} 260 & 80 & 20 \\ 80 & 80 & 20 \\ 20 & 20 & 30 \end{pmatrix}, \tag{A2}$$

where T represents the transpose of a matrix. The observations are available every 12 h and exactly at the same valid time as the 12-h background forecast. If the ensemble matrix is defined as

$$\mathbf{X}^f = (\mathbf{x}_1^f, \mathbf{x}_2^f, \ldots, \mathbf{x}_N^f), \tag{A3}$$

where the ensemble background forecasts are denoted by $\mathbf{x}_i^f$, with $N = 200$, then the ensemble perturbation matrix can be expressed as

$$\mathbf{X}'^f = \left(\mathbf{x}_1^f - \overline{\mathbf{x}^f}, \mathbf{x}_2^f - \overline{\mathbf{x}^f}, \ldots, \mathbf{x}_N^f - \overline{\mathbf{x}^f}\right), \tag{A4}$$

where $\overline{\mathbf{x}^f}$ denotes the arithmetic mean of the ensemble.

The background covariance matrix of the ensemble $\mathbf{X}^f$ can be calculated as

$$\mathbf{P}^f = \frac{1}{N-1}\mathbf{X}'^f\mathbf{X}'^{f\mathrm{T}}. \tag{A5}$$

The set of $\mathbf{y}_i$ ($i = 1, 2, \ldots, N$) represent a group of perturbed observations that corresponds to each previous ensemble forecast $\mathbf{x}_i^f$. They are defined as

$$\mathbf{y}_i = \mathbf{y} + \boldsymbol{\varepsilon}_i. \tag{A6}$$

The random perturbations $\boldsymbol{\varepsilon}_i$ follow the same covariance matrix as $\boldsymbol{\varepsilon}$. The analysis state is updated by combining the observation $\mathbf{y}_i$ with $\mathbf{x}_i^f$:

$$\mathbf{x}_i^a = \mathbf{x}_i^f + \mathbf{K}(\mathbf{y}_i - \mathbf{H}\mathbf{x}_i^f). \tag{A7}$$

The Kalman gain $\mathbf{K}$ is calculated by

$$\mathbf{K} = \mathbf{P}^f\mathbf{H}^{\mathrm{T}}(\mathbf{H}\mathbf{P}^f\mathbf{H}^{\mathrm{T}} + \mathbf{R})^{-1}. \quad \text{(A8)}$$

Note that $\mathbf{K}$ is actually a weighting measuring the ratio of the forecast and observational error covariance, which determines to what extent the background forecasts will be corrected to fit observations.

To avoid filter divergence due to undersampling and other issues, an inflation factor of 1.3 is applied to $\mathbf{X}'^f$. No covariance localization is used here since the 200 ensemble members filter out the bulk of spurious long-distance correlations that would be present with a smaller ensemble. The mean $\overline{\mathbf{x}^a}$ of the analysis ensemble $\mathbf{x}_i^a$ $(i = 1, 2, \ldots, N)$ is considered as the analyzed state used to initialize forecasts.

APPENDIX B

Local Dimension of Perturbations

The algorithm of the local dimension follows Patil et al. (2001). For a model field with uniformly distributed grid points, we consider a roughly square region of $L \times L$ with a gridpoint G in the center, where L is the number of grid points ($L = 5$ in our case). The $L \times L$ grid points of ensemble perturbation $\boldsymbol{\delta}_i$ $(i = 1, 2, \ldots, M)$ at one level form a local vector denoted by $\mathbf{c}_i$; M local column vectors then construct an $M \times N$ matrix ($N = L \times L$), $\mathbf{C} = (\mathbf{c}_1, \mathbf{c}_2, \ldots, \mathbf{c}_M)$. The $M \times M$ covariance matrix of $\mathbf{C}$ is $\mathbf{Q} = \mathbf{C}^{\mathrm{T}}\mathbf{C}$, where $\mathbf{C}^{\mathrm{T}}$ is the transpose of $\mathbf{C}$. By using the empirical orthogonal function analysis to matrix $\mathbf{Q}$, the singular values (square root of eigenvalues) can be computed and ordered by $\sigma_1 \geq \sigma_2 \geq \ldots \geq \sigma_M$. Then the local dimension over the region centered at gridpoint G can be derived by defining the following statistic on the singular values:

$$\psi(\sigma_1, \sigma_2, \ldots, \sigma_M) = \frac{\left(\sum_{i=1}^{M} \sigma_i\right)^2}{\sum_{i=1}^{M} \sigma_i^2}. \quad \text{(B1)}$$

The local dimensions for other regions can be similarly calculated.

REFERENCES

Abarbanel, H. D. I., R. Brown, and M. B. Kennel, 1991: Variation of Lyapunov exponents on a strange attractor. *J. Nonlinear Sci.*, **1**, 175–199, https://doi.org/10.1007/BF01209065.

Annan, J. D., 2004: On the orthogonality of bred vectors. *Mon. Wea. Rev.*, **132**, 843–849, https://doi.org/10.1175/1520-0493(2004)132<0843:OTOOBV>2.0.CO;2.

Aurell, E., G. Boffetta, A. Crisanti, G. Paladin, and A. Vulpiani, 1997: Predictability in the large: An extension of the concept of Lyapunov exponent. *J. Phys.*, **30A**, 1–26, https://doi.org/10.1088/0305-4470/30/1/003.

Balci, N., A. L. Mazzucato, J. M. Restrepo, and G. R. Sell, 2012: Ensemble dynamics and bred vectors. *Mon. Wea. Rev.*, **140**, 2308–2334, https://doi.org/10.1175/MWR-D-10-05054.1.

Benettin, G., L. Galgani, A. Giorgilli, and J. M. Strelcyn, 1980: Lyapunov characteristic exponents for smooth dynamical systems and for Hamiltonian systems: A method for computing all of them. Part 1: Theory. *Meccanica*, **15**, 9–20, https://doi.org/10.1007/BF02128236.

Bishop, C. H., and Z. Toth, 1999: Ensemble transformation and adaptive observations. *J. Atmos. Sci.*, **56**, 1748–1765, https://doi.org/10.1175/1520-0469(1999)056<1748:ETAAO>2.0.CO;2.

——, B. J. Etherton, and S. J. Majumdar, 2001: Adaptive sampling with the ensemble transform Kalman filter. Part I: Theoretical aspects. *Mon. Wea. Rev.*, **129**, 420–436, https://doi.org/10.1175/1520-0493(2001)129<0420:ASWTET>2.0.CO;2.

Bowler, N., 2006: Comparison of error breeding, singular vectors, random perturbations and ensemble Kalman filter perturbations strategies on a simple model. *Tellus*, **58A**, 538–548, https://doi.org/10.1111/j.1600-0870.2006.00197.x.

Buizza, R., and T. N. Palmer, 1995: The singular-vector structure of the atmospheric global circulation. *J. Atmos. Sci.*, **52**, 1434–1456, https://doi.org/10.1175/1520-0469(1995)052<1434:TSVSOT>2.0.CO;2.

——, P. L. Houtekamer, Z. Toth, G. Pellerin, M. Wei, and Y. Zhu, 2005: A comparison of the ECMWF, MSC, and NCEP global ensemble prediction systems. *Mon. Wea. Rev.*, **133**, 1076–1097, https://doi.org/10.1175/MWR2905.1.

Chen, B., J. Li, and R. Ding, 2006: Nonlinear local Lyapunov exponent and atmospheric predictability research. *Sci. China*, **49D**, 1111–1120, https://doi.org/10.1007/s11430-006-1111-0.

Corazza, M., E. Kalnay, D. J. Patil, S.-C. Yang, R. Morss, I. Szunyogh, B. R. Hunt, and J. A. Yorke, 2003: Use of the breeding technique to estimate the structure of the analysis "errors of the day." *Nonlinear Processes Geophys.*, **10**, 233–243, https://doi.org/10.5194/npg-10-233-2003.

Ding, R., and J. Li, 2007: Nonlinear finite-time Lyapunov exponent and predictability. *Phys. Lett.*, **364A**, 396–400, https://doi.org/10.1016/j.physleta.2006.11.094.

——, ——, and K. Ha, 2008: Nonlinear local Lyapunov exponent and quantification of local predictability. *Chin. Phys. Lett.*, **25**, 1919–1922, https://doi.org/10.1088/0256-307X/25/5/109.

Duan, W., M. Mu, and B. Wang, 2004: Conditional nonlinear optimal perturbation as the optimal precursors for El Nino–Southern Oscillation events. *J. Geophys. Res.*, **109**, D23105, https://doi.org/10.1029/2004JD004756.

Feng, J., R. Ding, D. Liu, and J. Li, 2014: The application of nonlinear local Lyapunov vectors to ensemble predictions in the Lorenz systems. *J. Atmos. Sci.*, **71**, 3554–3567, https://doi.org/10.1175/JAS-D-13-0270.1.

——, ——, J. Li, and D. Liu, 2016: Comparison of nonlinear local Lyapunov vectors with bred vectors, random perturbations and ensemble transform Kalman filter strategies in a barotropic model. *Adv. Atmos. Sci.*, **33**, 1036–1046, https://doi.org/10.1007/s00376-016-6003-4.

Goodman, J. C., and J. Marshall, 2002: Using neutral singular vectors to study low-frequency atmospheric variability. *J. Atmos. Sci.*, **59**, 3206–3222, https://doi.org/10.1175/1520-0469(2002)059<3206:UNSVTS>2.0.CO;2.

Greybush, S. J., E. Kalnay, M. J. Hoffman, and R. J. Wilson, 2013: Identifying Martian atmospheric instabilities and their

physical origins using bred vectors. *Quart. J. Roy. Meteor. Soc.*, **139**, 639–653, https://doi.org/10.1002/qj.1990.

Hamill, T. M., C. Snyder, and R. E. Morss, 2002: Analysis-error statistics of a quasigeostrophic model using three-dimensional variational assimilation. *Mon. Wea. Rev.*, **130**, 2777–2790, https://doi.org/10.1175/1520-0493(2002)130<2777:AESOAQ>2.0.CO;2.

Houtekamer, P. L., and H. L. Mitchell, 1998: Data assimilation using an ensemble Kalman filter technique. *Mon. Wea. Rev.*, **126**, 796–811, https://doi.org/10.1175/1520-0493(1998)126<0796:DAUAEK>2.0.CO;2.

Kalnay, E., 2003: *Atmospheric Modeling, Data Assimilation and Predictability*. Cambridge University Press, 341 pp.

——, M. Corazza, and M. Cai, 2002: Are bred vectors the same as Lyapunov vectors? Preprints, *Symp. on Observations, Data Assimilation, and Probabilistic Prediction*, Orlando, FL, Amer. Meteor. Soc., 173–177.

Keller, J. D., A. Hense, L. Kornblueh, and A. Rhodin, 2010: On the orthogonalization of bred vectors. *Wea. Forecasting*, **25**, 1219–1234, https://doi.org/10.1175/2010WAF2222334.1.

Li, J., and J. Chou, 1997: The existence of the atmosphere attractor. *Sci. China*, **40D**, 215–224, https://doi.org/10.1007/BF02878381.

——, and S. Wang, 2008: Some mathematical and numerical issues in geophysical fluid dynamics and climate dynamics. *Commun. Comput. Phys.*, **3**, 759–793.

——, and R. Ding, 2011: Temporal–spatial distribution of atmospheric predictability limit by local dynamical analogs. *Mon. Wea. Rev.*, **139**, 3265–3283, https://doi.org/10.1175/MWR-D-10-05020.1.

——, and ——, 2015: Seasonal and interannual weather prediction. *Encyclopedia of Atmospheric Sciences*, 2nd ed. Academic Press, 303–316.

Lorenz, E. N., 1963a: Deterministic nonperiodic flow. *J. Atmos. Sci.*, **20**, 130–141, https://doi.org/10.1175/1520-0469(1963)020<0130:DNF>2.0.CO;2.

——, 1963b: The predictability of hydrodynamic flow. *Trans. N. Y. Acad. Sci.*, **25**, 409–432, https://doi.org/10.1111/j.2164-0947.1963.tb01464.x.

——, and K. A. Emanuel, 1998: Optimal sites for supplementary weather observations: Simulation with a small model. *J. Atmos. Sci.*, **55**, 399–414, https://doi.org/10.1175/1520-0469(1998)055<0399:OSFSWO>2.0.CO;2.

Marshall, J., and F. Molteni, 1993: Toward a dynamical understanding of planetary-scale flow regimes. *J. Atmos. Sci.*, **50**, 1792–1818, https://doi.org/10.1175/1520-0469(1993)050<1792:TADUOP>2.0.CO;2.

Molteni, F., and T. N. Palmer, 1993: Predictability and finite time instability of the northern winter circulation. *Quart. J. Roy. Meteor. Soc.*, **119**, 269–298, https://doi.org/10.1002/qj.49711951004.

——, R. Buizza, T. N. Palmer, and T. Petroliagis, 1996: The new ECMWF ensemble prediction system: Methodology and validation. *Quart. J. Roy. Meteor. Soc.*, **122**, 73–119, https://doi.org/10.1002/qj.49712252905.

Mu, M., 2013: Methods, current status, and prospect of targeted observation. *Sci. China Earth Sci.*, **56**, 1997–2005, https://doi.org/10.1007/s11430-013-4727-x.

——, W. S. Duan, and B. Wang, 2003: Conditional nonlinear optimal perturbation and its applications. *Nonlinear Processes Geophys.*, **10**, 493–501, https://doi.org/10.5194/npg-10-493-2003.

——, ——, and ——, 2007: Season-dependent dynamics of nonlinear optimal error growth and El Niño-Southern Oscillation predictability in a theoretical model. *J. Geophys. Res.*, **112**, D10113, https://doi.org/10.1029/2005JD006981.

——, F. F. Zhou, and H. L. Wang, 2009: A method to identify the sensitive areas in targeting for tropical cyclone prediction: Conditional nonlinear optimal perturbation. *Mon. Wea. Rev.*, **137**, 1623–1639, https://doi.org/10.1175/2008MWR2640.1.

Newman, C. E., P. L. Read, and S. R. Lewis, 2004: Investigating atmospheric predictability on Mars using breeding vectors in a general-circulation model. *Quart. J. Roy. Meteor. Soc.*, **130**, 2971–2989, https://doi.org/10.1256/qj.03.209.

Oseledec, V. I., 1968: A multiplicative ergodic theorem: Lyapunov characteristic numbers for dynamical systems. *Trans. Moscow Math. Soc.*, **19**, 197–231.

Patil, D. J., B. R. Hunt, E. Kanlay, J. A. Yorke, and E. Ott, 2001: Local low dimensionality of atmospheric dynamics. *Phys. Rev. Lett.*, **86**, 5878–5881, https://doi.org/10.1103/PhysRevLett.86.5878.

——, I. Szunyogh, A. V. Zimin, B. R. Hunt, E. Ott, E. Kalnay, and J. A. Yorke, 2003: Local low dimensionality and relation to effects of targeted weather observations. *Proc. Seventh Experimental Chaos Conf.*, San Diego, CA, American Institute of Physics, 139–153, https://doi.org/10.1063/1.1612207.

Peña, M., Z. Toth, and M. Wei, 2010: Controlling noise in ensemble data assimilation schemes. *Mon. Wea. Rev.*, **138**, 1502–1512, https://doi.org/10.1175/2009MWR2854.1.

Primo, C., M. A. Rodriguez, and J. M. Gutierrez, 2008: Logarithmic bred vectors. A new ensemble method with adjustable spread and calibration time. *J. Geophys. Res.*, **113**, D05116, https://doi.org/10.1029/2007JD008998.

Ruelle, D., and F. Takens, 1971: One the nature of turbulence. *Commun. Math. Phys.*, **20**, 167–192, https://doi.org/10.1007/BF01646553.

Szunyogh, I., E. Kainay, and Z. Toth, 1997: A comparison of Lyapunov vectors and optimal vectors in a low-resolution GCM. *Tellus*, **49A**, 200–227, https://doi.org/10.3402/tellusa.v49i2.14467.

Toth, Z., and E. Kalnay, 1993: Ensemble forecasting at NMC: The generation of perturbations. *Bull. Amer. Meteor. Soc.*, **74**, 2317–2330, https://doi.org/10.1175/1520-0477(1993)074<2317:EFANTG>2.0.CO;2.

——, and ——, 1997: Ensemble forecasting at NCEP: The breeding method. *Mon. Wea. Rev.*, **125**, 3297–3318, https://doi.org/10.1175/1520-0493(1997)125<3297:EFANAT>2.0.CO;2.

——, I. Szunyogh, and E. Kalnay, 1999: Comments on ''Notes on the appropriateness of 'bred modes' for generating initial perturbations used in ensemble prediction.'' *Tellus*, **51A**, 442–449, https://doi.org/10.3402/tellusa.v51i3.13594.

Trevisan, A., and R. Legnani, 1995: Transient error growth and local predictability: A study in the Lorenz system. *Tellus*, **47A**, 103–117, https://doi.org/10.3402/tellusa.v47i1.11496.

——, and F. Uboldi, 2004: Assimilation of standard and targeted observations within the unstable subspace of the observation–analysis–forecast cycle system. *J. Atmos. Sci.*, **61**, 103–113, https://doi.org/10.1175/1520-0469(2004)061<0103:AOSATO>2.0.CO;2.

Uboldi, F., A. Trevisan, and A. Carrassi, 2005: Developing a dynamically based assimilation method for targeted and standard observations. *Nonlinear Processes Geophys.*, **12**, 149–156, https://doi.org/10.5194/npg-12-149-2005.

Vannitsem, S., and C. Nicolis, 1997: Lyapunov vectors and error growth patterns in a T21L3 quasigeostrophic model. *J. Atmos. Sci.*, **54**, 347–361, https://doi.org/10.1175/1520-0469(1997)054<0347:LVAEGP>2.0.CO;2.

——, and ——, 1998: Dynamics of fine-scale versus averaged observables in a T21L3 quasi-geostrophic model. *Quart. J. Roy. Meteor. Soc.*, **124**, 2201–2226, https://doi.org/10.1002/qj.49712455103.

Wang, X., and C. Bishop, 2003: A comparison of breeding and ensemble transform Kalman filter ensemble forecast schemes. *J. Atmos. Sci.*, **60**, 1140–1158, https://doi.org/10.1175/1520-0469(2003)060<1140:ACOBAE>2.0.CO;2.

Wei, M., and Z. Toth, 2003: A new measurement of ensemble performance: Perturbation versus error correlation analysis (PECA). *Mon. Wea. Rev.*, **131**, 1549–1565, https://doi.org/10.1175//1520-0493(2003)131<1549:ANMOEP>2.0.CO;2.

——, and J. S. Frederiksen, 2004: Error growth and dynamical vectors during Southern Hemisphere blocking. *Nonlinear Processes Geophys.*, **11**, 99–118, https://doi.org/10.5194/npg-11-99-2004.

——, Z. Toth, R. Wobus, Y. Zhu, C. H. Bishop, and X. Wang, 2006: Ensemble transform Kalman filter-based ensemble perturbations in an operational global prediction system at NCEP. *Tellus*, **58A**, 28–44, https://doi.org/10.1111/j.1600-0870.2006.00159.x.

——, ——, ——, and ——, 2008: Initial perturbations based on the ensemble transform (ET) technique in the NCEP global operational forecast system. *Tellus*, **60A**, 62–79, https://doi.org/10.1111/j.1600-0870.2007.00273.x.

Wolf, A., J. B. Swift, H. L. Swinney, and J. A. Vastano, 1985: Determining Lyapunov exponents from a time series. *Physica D*, **16**, 285–317, https://doi.org/10.1016/0167-2789(85)90011-9.

Yang, S. C., C. Keppenne, M. R. Rienecker, and E. Kalnay, 2009: Application of coupled bred vectors to seasonal-to-interannual forecasting and ocean data assimilation. *J. Climate*, **22**, 2850–2870, https://doi.org/10.1175/2008JCLI2427.1.

Zhang, J., W. Duan, and X. Zhi, 2015: Using CMIP5 model outputs to investigate the initial errors that cause the ''spring predictability barrier'' for El Niño events. *Sci. China Earth Sci.*, **58**, 685–696, https://doi.org/10.1007/s11430-014-4994-1.